ORIGINAL ARTICLE

CrossMark

Oxy-dry reforming of propane over Ce-promoted Co–Ni/Al$_2$O$_3$ catalyst

Faisal M. Althenayan[1] · Adesoji A. Adesina[2]

Abstract

This paper reports the production of syngas from two types of O$_2$-assisted dry reforming of propane, namely oxidative (O$_2$-dosed) dry reforming (ODR) and dry (CO$_2$-dosed) partial oxidation (DPOX). Reaction runs were conducted over alumina-supported bimetallic Co–Ni promoted with CeO$_2$ at 120 kPa and 793–893 K. Ceria promotion improved the carbon deposition resilience of the Co–Ni catalyst. Physicochemical attributes were obtained from liquid N$_2$ adsorption, H$_2$ chemisorption and temperature-programmed desorption runs for NH$_3$, CO$_2$, CH$_4$ and C$_3$H$_8$. Rate behavior under ODR, DPOX and pure dry reforming could be described consistently with empirical models that are structurally similar to Langmuir–Hinshelwood type relations. Inferences from these models allowed the postulation of the same overall reaction network for the three types of reactions albeit with variation in rate-controlling steps depending on the different product species. On the whole, DPOX seemed to be a superior option for the manufacturing of syngas for downstream olefin FT production due to reduced variability in the H$_2$:CO ratio and the closeness to unity (0.72–0.95) of the exiting syngas over the range of O$_2$ partial pressure used.

Keywords Dry reforming · Partial oxidation · Propane · Ceria promotion · Syngas · Co–Ni catalyst

Introduction

Synthesis gas (H$_2$/CO) is the primary feedstock for clean fuels manufacturing in a variety of gas-to-liquid (GTL) conversion processes [16, 21, 28]. Although steam reforming (SR) of hydrocarbons is most commonly employed, the partial oxidation (POX), and dry reforming (DR) routes have also been discussed [23, 27]. In particular, autothermal reforming [10, 11, 17, 18] which combines the exothermic POX with the endothermic SR reactions in a single reactor module in order to reduce overall energy demand and minimize carbon deposition has also attracted considerable attention within the past decade [12, 13, 19]. However, with the recent interest in the role of greenhouse gases on climate change and possible carbon tax on manufacturing plants,

development of efficient technologies for CO$_2$ utilization in the petrochemicals and gas processing industries has taken on added urgency. Thus, the CO$_2$ (dry) reforming option for syngas production has assumed a central stage in new green technology initiatives [1]. Similar to steam reforming, it is also an endothermic reaction. Nevertheless, the product H$_2$:CO ratio is lower than that from SR and more suitable for downstream olefin or GTL synthesis.

In this study, the co-feeding of oxygen with the CO$_2$ and hydrocarbon as reactants to the reformer has been proposed in order to take advantage of the exothermicity of the accompanying hydrocarbon oxidation to reduce energy requirement for the dry reforming. In particular, O$_2$ addition will also improve material economy through reactive excoriation of the carbon residue that inevitably accompanies dry reforming. This is especially relevant with C$_{2+}$ alkanes as the hydrocarbon source due to a greater propensity for carbon laydown than with CH$_4$. A further benefit of this approach in comparison with the autothermal reforming is that the additional energy for steam generation is avoided. The combined pure DR and POX of propane are given by

$$C_3H_8 + \frac{3}{2}CO_2 + \frac{3}{4}O_2 = \frac{9}{2}CO + 4H_2 \tag{1a}$$
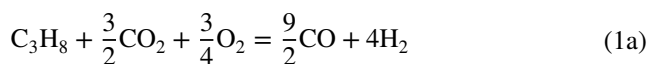
Work done while authors were with the Reactor Engineering & Technology Group, School of Chemical Engineering, University of New South Wales, Sydney, NSW Australia 2052.

✉ Adesoji A. Adesina
ceo@atodatech.com

1 Saudi Aramco, Research & Development Dept, P.O. Box 5000, Dhahran 31311, Kingdom of Saudi Arabia

2 ATODATECH LLC, Pasadena, CA 91101, USA

Thus, for the oxy-dry reforming operation (where the relative partial pressure of O_2 and CO_2 may be varied to achieve different levels of oxygen-assisted reforming), the reaction rewrites in general form as:

$$C_3H_8 + (3 - 2\gamma)CO_2 + \gamma O_2 = (6 - 2\gamma)CO + 4H_2 \qquad (1b)$$
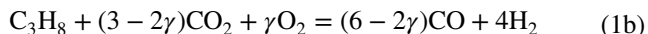
where γ is the amount of O_2 supplied per mole of C_3H_8 fed with $\gamma = 0$ for pure dry reforming and $\gamma = 1.5$ for the strict partial oxidation option. Given that pure propane DR is an endothermic reaction ($\Delta H_{298} = 622$ kJ mol^{-1}) while propane POX is exothermic ($\Delta H_{298} = -227$ kJ mol^{-1}), the heat of reaction, ΔH, for Eq. (1b) may vary from positive to negative values for $0 \leq \gamma \leq 1.5$ in addition to being a function of temperature, T. Indeed, $\Delta H(T)$, may be given by

$$\Delta H(T) = \mu_0 + R_g \left(\mu_1 T + \frac{\mu_2}{2}T^2 + \frac{\mu_3}{3}T^3 - \frac{\mu_4}{T} \right)\Big|_{298}^{T} \text{(kJ mol}^{-1}\text{)}$$
$$(2)$$

for $373 \leq T \leq 1073$ K where R_g is the universal gas constant (8.413 J mol^{-1}K^{-1}) and μ_0 to μ_4 are dependent on γ as displayed in Table 1. It is immediately evident that Eq. (1b) yields theoretical H_2:CO ratio of $2/(3-\gamma)$ which is more suitable for downstream Fischer–Tropsch synthesis or olefin production plant (i.e., 0.67–1.33 for realistic values of γ) than the higher values (> 3) obtained from typical steam reforming operation. Furthermore, using the parameter expressions provided on Table 1, Eq. (2) may be readily simplified to the linear form:

$$\Delta H(T) = \left(0.1951 - 6.2 \times 10^{-3}\gamma\right)T + (542.72 - 558.1\gamma)$$
$$(3)$$

with an error bound of $\pm 5\%$ (compared to its full nonlinear version). However, the possible side reactions such as reverse water–gas shift reaction, carbon deposition, H_2 and CO oxidation may impact upon the true product distribution. Therefore, a key objective of this investigation is to obtain empirical O_2 partial pressure in the feed that will optimize the H_2:CO product ratio while maintaining maximal reaction rate and minimal carbon laydown. Promotion of the Co–Ni catalyst with ceria has been adopted in the present investigation because rare-earth oxides have been found to reduce carbon deposition during hydrocarbon dehydrogenation [5], steam reforming [20, 29] and dry reforming [8, 9].

Table 1 Values of thermodynamic parameters in Eq. (1b)

Parameter	Expression
μ_0	$626.3 - 565.96\gamma$
μ_1	$15.36 + 0.52\gamma + 3.18 \times 10^{-17}(1 - 0.667\gamma)$
μ_2	$-26.2 \times 10^{-3} - 4 \times 10^{-4}\gamma$
μ_3	8.543×10^{-6}
μ_4	$36.11 \times 10^4 - 6.73 \times 10^4\gamma$

Experimental details

The ceria-promoted Co–Ni catalyst was prepared by co-impregnation of the aqueous solution containing calculated amounts of Co(NO$_3$)$_2$, Ni(NO$_3$)$_2$ and Ce(NO$_3$)$_3$ onto γ-alumina (support) which had been previously treated at 1073 K for 6 h. The nitrate addition was followed by 3 h of stirring at 303 K (at constant pH of two) using a computer-controlled Mettler–Toledo Excellence titrator (model T90) and subsequent 24 h drying of the slurry in an oven was performed at 403 K. The resulting solid containing 2.5Ce:5Co:10Ni (wt % basis) on alumina was further calcined at 1073 K for 5 h at 5 K min^{-1}. The calcined solid was then crushed and sieved to 180–250 μm particles for characterization and reactor studies.

The BET surface area and pore volume for the catalyst were obtained from liquid N_2 adsorption–desorption measurements at 77 K on Quantachrome Autosorb-1 unit. H_2 chemisorption was carried out on Micromeritics AutoChem 2910 (equipped with a thermal conductivity detector, TCD, and gas ports with mass flow controllers for preparation, carrier and analysis gases) to determine metal dispersion and particle size while acid and basic site concentration and strength were obtained on the same instrument using NH$_3$ and CO_2 temperature-programmed desorption (TPD) at 973 K for 4 different heating rates (15, 20, 25, 30 K min^{-1}). TPD runs were also performed for C_3H_8 and CH_4 under identical conditions to determine the adsorption characteristics (heat of desorption and site coverage) of these species, especially since CH_4 may be produced via direct C_3H_8 decomposition during reforming. Metal oxide phase identification was performed on ThermoCahn TG-2121 TGA unit under H_2-temperature-programmed reduction (TPR). TPR runs employed 50% H_2/Ar mixture flowing at 55 ml min^{-1} at 973 K under a temperature ramp of 10 K min^{-1}. XRD analysis was also conducted on a Philips X'pert system using an Ni-filtered Cu K$_\alpha$ radiation ($\lambda = 1.542$ Å) at 40 kV and 30 mA to complement H_2-TPR data. Actual elemental composition of the fresh catalyst was determined via XRF analysis. The residual total organic carbon (TOC) content on used catalyst specimens was obtained from a Shimadzu Total Organic Carbon Analyzer (solid module SM-5000A).

Catalyst evaluation runs for the Ce-promoted catalyst were carried out in a 15 mm ID quartz fixed-bed reactor at temperatures between 793 and 893 K and constant pressure of 120 kPa. Prior to each run, the catalyst (ca. 0.5 g) was reduced in H_2 for 2.5 h. Feed gas to the reactor contained CO_2, C_3H_8 and O_2 at a total flow rate of 100 ml min^{-1}(at 298 K). In one set of experiments, feed with different CO_2:C_3H_8 ratio, R_{CO_2} (from 0 to 9) but regulated to keep

a constant feed O_2:C_3H_8 ratio, R_{O_2}, of 0.75 was employed. This was termed, the oxidative dry reforming (ODR) or O_2-dosed dry reforming set since CO_2 partial pressure was varied. The fixed R_{O_2} value of 0.75 corresponds to the stoichiometric requirement in Eq. (1a). The influence of oxygen partial pressure was investigated in the second set of runs by varying the feed O_2:C_3H_8 ratio, R_{O_2}, from 0 to 1.5 with the feed CO_2 content, R_{CO_2} kept constant at 1.5 for each run [the stoichiometric coefficient of CO_2 in Eq. (1a)]. This second set of runs was referred to as the dry partial oxidation (DPOX) or CO_2-dosed POX. Feed mixture composition in all runs was carefully chosen to be well outside the hydrocarbon explosion limits. Additional experimental details are provided in a previous paper [3].

Results and discussion

Properties of fresh and used catalyst samples

XRF analysis revealed an elemental composition of the promoted catalyst as 2.6 wt % Ce, 5.5 wt % Co and 10.5 wt %

**Table 2** Physical properties of the undoped and Ce-promoted catalyst

Ce loading (wt %)	0	2.5
BET Area, S_T (m^2 g^{-1})	122	121
Pore volume, PV (ml g^{-1})	0.53	0.55
Metal dispersion, D (%)	0.74	0.74
Metal area, S_m (m^2 g^{-1})	0.74	0.85
Crystallite size from H_2 chemisorption, d (nm)	135	142
Crystallite size from XRD data, d (nm)	122	147

Ni and balance (others) in reasonable agreement with the intended recipe of 5Co:10Ni and 2.5Ce:5Co:10Ni. However, traces of I, Yb, Si, Th, Te, Fe in the range 0.0043–1.09 wt % were probably due to original impurities in the AR grade Sigma-Aldrich chemicals.

BET and pore volume data displayed in Table 2 suggest that the addition of ceria to the Co–Ni/Al_2O_3 catalyst did not have any marked effect on its porosity or surface area— an indication of negligible increase in crystallite size. XRD runs were performed on a Phillips X'Pert X-ray diffractometer using Ni-filtered Cu$K\alpha$ radiation ($\lambda = 1.542$ Å) at 40 kV and 30 mA. The X'Pert Pro software was used for the qualitative determination of the metallic oxide phases. The X-ray diffraction patterns of calcined catalysts (cf. Fig. 1) showed that both ceria-promoted and undoped Co–Ni catalysts contained similar cobalt and nickel oxides, with $NiCo_2O_4$ ($2\theta = 31°$ and $36.6°$) and Co_3O_4 at $2\theta = 31.2°$ and $36.7°$ while NiO is located at $2\theta = 43.2°$. The metal aluminates, $CoAl_2O_4$ ($2\theta = 36.7°$) as well as $NiAl_2O_4$ ($2\theta = 37°$; $44.8°$), exhibited strong intensities but the CeO_2 was identified as a separate oxide phase on the ceria-containing catalyst at $2\theta = 28.6°$. The absence of Ce aluminate and Ce–Co–Ni oxide phases indicates negligible perovskite formation. H_2 chemisorption data collected at 383 K and detailed in Table 2 revealed that the metal particle size and dispersion were barely affected by the addition of ceria suggesting that the latter was unreduced under the conditions employed.

Average crystallite size for all the metal oxides computed from Scherrer equation for the XRD data was 122.2 nm (undoped) and 147.1 nm (promoted). These values compare well with those from H_2 uptake data. H_2-TPR profile shown in Fig. 2 suggests the presence of nearly identical metal phases in both types of catalyst. The peak at 401 K may be attributed

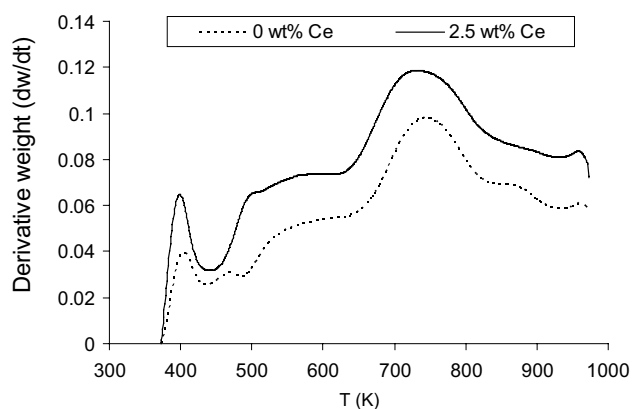**Fig. 1** X-ray diffraction patterns for the Co–Ni catalyst and the Ce-promoted counterpart
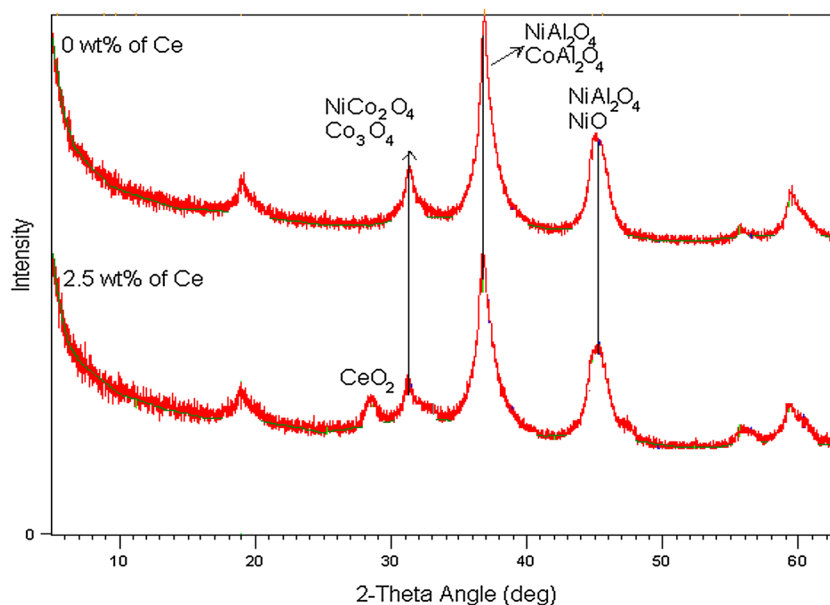
Fig. 2 TPR patterns of fresh 0 and 2.5 wt % Ce–5Co:10Ni catalyst samples

Table 3 Catalyst properties arising from temperature-programmed desorption of NH_3 and CO_2 (acid-base attributes) as well as C_3H_8 and CH_4 for the catalysts

Ce loading wt %	0	2.5
Acidic site concentration (mol m_{BET}^{-2})$\times 10^6$	6.8	6.1
Basic site concentration (mol metal-mm$_{BET}^{-2}$)$\times 10^7$	1.9	3.5
Acidic:basic site ratio	35	17
Heat of desorption for NH_3, E_d, (kJ mol^{-1})	104.5	73.5
Heat of desorption for CO_2, E_d, (kJ mol^{-1})	66.5	78.5
Site concentration for C_3H_8 adsorption (mol m_{BET}^{-2})$\times 10^6$	3.4	3.8
Site concentration for CH_4 adsorption (mol m_{BET}^{-2})$\times 10^6$	11.4	19.5
Heat of desorption for C_3H_8, E_d, (kJ mol^{-1})	102	74
Heat of desorption for CH_4, E_d, (kJ mol^{-1})	82	46

to the removal of interstitial water. The principal broad peak at about 725 K is due to the reduction of a key metal oxide phase containing Co_3O_4, $NiCo_2O_4$ and NiO. However, the low temperature shoulder peaks (473–513 K) may be ascribed to the presence of XRD-amorphous Ni_2O_3 and Co_2O_3 (arising from the thermodynamically feasible $2NiO + Co_3O_4 + CoO + O_2 \leftrightarrow Ni_2O_3 + 2Co_2O_3$ at $T \geq 673$ K) while the higher temperature peaks suggest the reduction of the Ni-Co aluminates (at 973 K). Since CeO_2 is irreducible below 1000 K, a peak corresponding to ceria reduction was absent from the TPR profile. The results of NH_3-TPD summarized in Table 3 indicate that both catalysts have relatively weak acid sites characterized by NH_3 heat of desorption, E_d, of 104.5 kJ mol^{-1} (for unpromoted) and 73.5 kJ mol^{-1} (Ce-doped) characteristic of Lewis acid sites with peak temperature below 673 K [6]. Interestingly, the acid site concentrations on both catalysts are close (6–7 µmol m^{-2}) implicating the location of acid sites at the Ni (and Co)-support boundary since they have nearly identical composition and phases on both catalysts. However, the CO_2-TPD data suggest that the basic site concentration on

the promoted catalyst (0.35 µmol m^{-2}) is nearly twice that of the undoped specimen (0.19 µmol m^{-2}). Basic sites may be the contiguous conjugate centers of the metal-support boundary acid sites in the Ni-Co/Al_2O_3 catalyst. The ceria phase in the promoted sample also offers additional basic sites due to free oxygen at the CeO_2 surface. Moreover, while the acid site strength on the ceria-containing catalyst is somewhat weaker than the undoped counterpart, the latter appears to have weaker basic site strength (66.5 kJ mol^{-1}) than the promoted sample (78.5 kJ mol^{-1}). Thus, the ratio of the acid:basic site density in the undoped catalyst is about twice that of the ceria-promoted sample confirming the latter's stronger basic character.

Table 3 also shows the results of the C_3H_8 and CH_4-TPD runs at 1023 K using four heating rates from 15 to 30 K min^{-1}. It is apparent that the surface capacity for C_3H_8 adsorption is similar for both catalysts (3.4 and 3.8 µmol m^{-2} undoped and promoted samples, respectively) suggesting that the reduced metal crystallites are the C_3H_8 adsorption sites. Nonetheless, the heat of desorption for the reactant is significantly different with 102 kJ mol^{-1} for the Co–Ni catalyst and 74 kJ mol^{-1} for the Ce–Co–Ni system. The smaller C_3H_8 desorption strength on the promoted catalyst implicates a reduced carbonaceous residue on the ceria-containing sample. This trend is also reinforced by the CH_4-TPD runs which gave heat of desorption values of 82 and 46 kJ mol^{-1} for the unpromoted and promoted catalysts as may be seen on Table 3. The somewhat higher surface capacity for CH_4 adsorption on the promoted catalyst (19.5 µmol m^{-2}) than the Co–Ni catalyst (11.4 µmol m^{-2}) suggests the possibility of additional CH_4 chemisorption on ceria sites. Furthermore, the ratio of surface site concentration between CH_4 and C_3H_8 on the unpromoted catalyst is 3.35 (i.e., 11.4/3.4) indicating that C_3H_8 may reasonably fragment into three CH_y adspecies (not necessarily in a single step) on the catalyst surface. However, the enhanced adsorption capacity due to ceria addition is also consistent with a surface site ratio (between CH_4 and C_3H_8) of about 5 (19.5/3.8 = 5.13) for the promoted catalyst. Perhaps the ceria phase offered adsorption centers that are more suitably sized for CH_4 than C_3H_8 (since CH_4 is smaller at 40 nm than the C_3H_8 molecule at 49 nm). Interestingly, an increase in the surface adsorption capacity for CH_4 as compared to C_3H_8 (ca. 70%) in the promoted catalyst corresponds reasonably well with the area coverage based on the species size. These attributes foreshadow superior carbon resistance character due to ceria promotion.

Oxidative reforming runs: effect of feed CO_2:C_3H_8 ratio (R_{CO_2})

Although several studies have focused on the effect of catalyst on dry reforming [12], there is a paucity of information on the kinetic implications of the rate data and plausible

empirical models. The latter may be culled from the commercially available modeling software following optimized data regression. Figure 3a shows the rate behavior (for H_2, CH_4 and C_3H_8) as a function of the principal reactant ratio, R_{CO_2} in the feed while the oxygen content was kept constant at $R_{O_2} = 0.75$ for each run. Since the stoichiometric feed CO_2:C_3H_8 ratio required by Eq. (1b) is 1.5 (i.e., 3-2γ), it is evident that the range of R_{CO_2} employed (0–9) included sub- and supra-stoichiometric conditions. All three species displayed a hyperbolic rate decrease with R_{CO_2} suggesting a pseudo-first-order dependency on feed composition. The initial high H_2 production may be attributed strong dissociative C_3H_8 chemisorption on metal sites at the high C_3H_8 partial pressure (corresponding to low R_{CO_2} values). The Ni-support boundary contains acid sites where hydrogen abstraction from the alkane molecule can take place producing C_xH_{1-x} type unsaturated carbonaceous species. The similarity in the R_{CO_2} dependency of H_2, CH_4 rate curves implicates the direct

formation of these species from C_3H_8 adsorption. Thus, the appropriate empirical rate equation may be given as:

$$r_i = \frac{r_i^0}{\left[1 + K_{oxi}R_{CO_2}\right]} \quad (4)$$

where the numerator, r_i^0, corresponds to the consumption or net production rate of these species ($i = H_2$, CH_4 and C_3H_8) for the direct partial oxidation of propane at $R_{CO_2} = 0$ (with $R_{O_2} = 0.75$) while K_{oxi} is an empirical constant. Although Eq. (4) was not derived from formal mechanistic considerations, it is structurally similar to a conventional Langmuir–Hinshelwood rate model where the denominator is the sum of adsorption terms which constitutes the resistance to reaction and the numerator, r_i^0, is the driving force and depends on R_{O_2} (i.e., the O_2 partial pressure) in this case. Indeed, K_{oxi} may be regarded as the ratio of adsorption equilibrium constants for CO_2 and C_3H_8 since both are implicated in the feed variable, R_{CO_2}. Estimates of the parameters in Eq. (4) based on the nonlinear regression of the rate data (using SigmaPlot 10 modeling software) are summarized in Table 4.

In Fig. 3b, both CO production and CO_2 consumption curves revealed a turning point at R_{CO_2} between 2 and 3, which is above the stoichiometric value of 1.5 indicating that CO_2 is not only less strongly adsorbed than C_3H_8 on the catalyst, but was also involved in CO formation. The adsorption of CO_2 on weak basic sites is evidenced from Table 3. These sites are present on both unpromoted and ceria-containing (0.35 μmol m^{-2}_{BET}) catalysts in a ratio of about 1:2. The higher heat of desorption on the promoted catalyst is consistent with the formation of a bidentate carbonate species on the ceria catalyst where surface oxygen species most likely enhanced CO_2 adsorption [26]. The bidentate species would react with surface carbon during dry reforming yielding lower carbon formation compared to the unpromoted Co–Ni catalyst. The separate ceria phase is evident from X-ray diffractogram. The weak adsorption of CO_2 would require much higher gas phase CO_2 partial pressure to ensure favorable coverage in order to compensate for the stronger chemisorption of C_3H_8 for the surface reaction to proceed
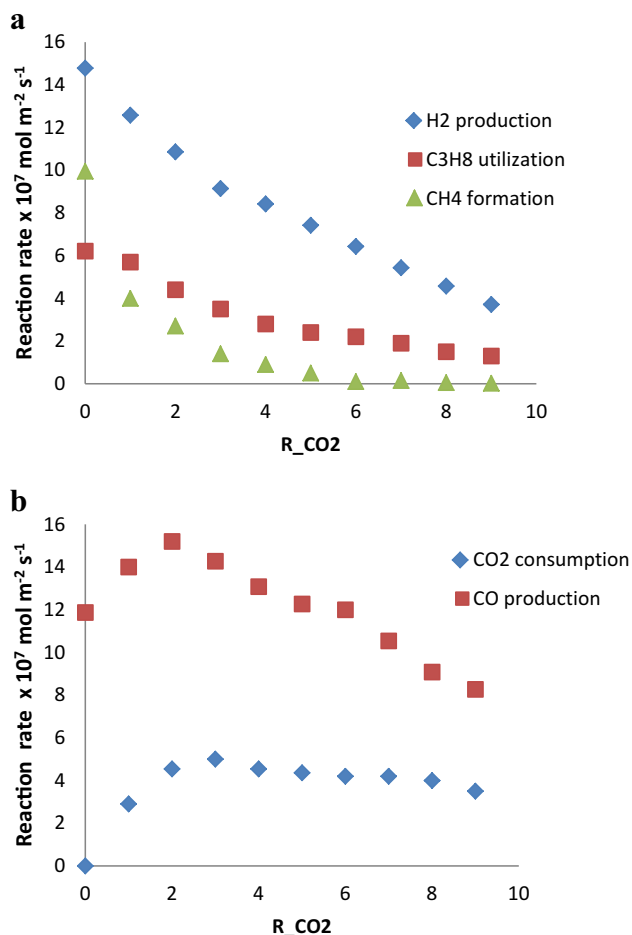
Fig. 3 a Rate profiles for H_2 and CH_4 production and C_3H_8 consumption during oxidative reforming using R_{O_2} of 0.75 at 873 K. **b** Rate profiles for CO production and CO_2 consumption during oxidative reforming using R_{O_2} of 0.75 at 873 K

Table 4 Estimates of parameters for Eq. (4) for describing the rate profiles for H_2, CH_4 and C_3H_8 during oxidative dry reforming

Species	$r_i^0 \times 10^7$ (mol m^{-2} s^{-1})	K_{oxi}	Correlation coefficient
H_2	15.26	0.237	0.99
CH_4	10.02	1.905	0.99
C_3H_8	6.65	0.324	0.98

$i = H_2$, CH_4 and C_3H_8

Table 5 Estimates of parameters for Eq. (5) for the CO and CO_2 rate profiles during oxidative dry reforming

Species	$r_j^0 \times 10^7$ (mol m^{-2} s^{-1})	$k_1 \times 10^7$ (mol m^{-2} s^{-1})	k_2	Correlation coefficient
CO	11.68	14.29	0.33	0.97
CO_2	0	5.46	0.29	0.99

$j = $ CO and CO_2

at reasonable rate. This would account for the appearance of the CO and CO_2 rate maxima beyond the stoichiometric value ($R_{CO_2} = 1.5$) during reforming. As a result, the rate behavior for both CO production and CO_2 consumption may be captured by the unimodal relation:

$$r_j \left[\text{or} (-r_j) \right] = \frac{[r_j^0 + k_1 R_{CO_2}]}{[1 + k_2 R_{CO_2}]^2} j = \text{CO or } CO_2 \quad (5)$$

where k_1 is a pseudo-kinetic constant and k_2 is combination of adsorption equilibrium constants in the steps for CO formation and CO_2 utilization rates, while r_j^0 is the rate for species j when $R_{CO_2} = 0$ (i.e., at $R_{O_2} = 0.75$). Nonlinear parameter estimation provided the values displayed in Table 5.

Spectroscopic studies ([25]; [24]) have shown that propane dissociatively chemisorbs on metal sites yielding unsaturated carbonaceous species, C_xH_{1-x}, (or atomic C) and H adatoms. Moreover, both H_2 and CH_4 may further react with CO_2 and O_2 contributing to the overall exponential decrease in their respective production rates with increasing R_{CO_2} value. Even so, the declining CO production rate with increasing CO_2 partial pressure ($R_{CO_2} > 3$) indicates a reduction in the surface concentration of the precursor carbonaceous species during reforming. The reactivity of the carbonaceous species is also dependent on its composition (value of x) and age on the catalyst surface as observed by Hardiman et al. [14]. The CO_2 consumption rate profile (cf. Fig. 3b) has been corrected for the CO_2 supplied to the reactor. The slow drop in its utilization rate after $R_{CO_2} > 3$ may be associated with the low concentration of surface carbonaceous species occasioned by the reduced C_3H_8 partial pressure as well as catalyst activity loss due to metal site re-oxidation at high R_{CO_2} and in the presence of O_2 via

$$C_3H_8 + 5CO_2 + \frac{(z-1)}{2}O_2 + \text{Ni} - \text{Co} = 8CO + 4H_2 + \text{NiO} - \text{CoO}_z \quad (6)$$
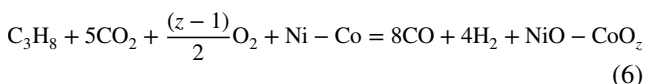
where Ni–Co is the reduced metal catalyst and NiO–CoO$_z$ is the oxidized catalyst ($0 \leq z \leq 1.5$) to accommodate the multiple oxidation states of Co. Indeed, the formation of NiCo$_2$O$_4$ and Co$_3$O$_4$ (NiO–CoOz for $z = 1.5$ and 1.33, respectively) is consistent with thermodynamics and the XRD phases observed in Fig. 2. Interestingly, CH_4 which may also be

formed from the hydrogenation of the C_xH_{1-x} surface precursor reached nearly negligible rates at $R_{CO_2} \geq 5$ suggesting minimal surface carbonaceous coverage at high CO_2 partial pressure. Figure 4 illustrates the product ratio behavior with respect to the feed composition. It is apparent that the H_2:CO curve approached an asymptotic limit of 0.48 at $R_{CO_2} \geq 5$. This limiting value is in agreement with an estimate of 0.5 implicated in Eq. (6). Consistent with the preceding discussion, the CH_4:CO and CH_4:H_2 ratio are also decay curves. Hence, the product ratio profile may be captured by the 3-parameter hyperbolic decay model:

$$PR_{ij} = PR_{ij}^\infty + \frac{\alpha_{ij}}{[1 + \beta_{ij} R_{CO_2}]} \quad (7)$$

where PR_{ij} is the product ratio of species, i to j, PR_{ij}^∞ is the product ratio of i to j at infinite (high) CO_2 partial pressure (i.e., $R_{CO_2} \geq 5$), with α_{ij} and β_{ij} as empirical rate constants associated with the formation of species i and j. These estimates are supplied in Table 6. Since PR_{ij}^∞ is zero for both CH_4:CO and CH_4:H_2, it may be considered as the contribution from the non-catalytic gas–solid reaction described in Eq. (6). Nonetheless, at $R_{CO_2} = 0$, the partial oxidation of C_3H_8 would have proceeded with $R_{O_2} = 0.75$ which is smaller than the stoichiometric requirement of 1.5, obtained from the reaction:

$$C_3H_8 + \frac{3}{2}O_2 = 3CO + 4H_2 \quad (8)$$
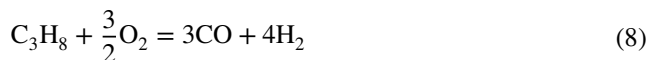
Consequently, an H_2:CO ratio of 1.25 obtained from Fig. 4 suggests that the ceria promoter may have served as a source of supplementary oxygen and, hence, its closeness to the theoretical value of 1.33 based on Eq. (8). The participation
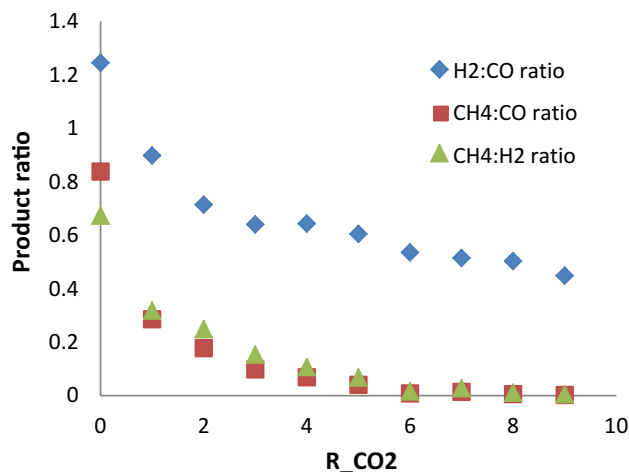

Fig. 4 Product ratio as a function of the feed composition under oxidative dry reforming of propane at 873 K with R_{O_2} of 0.75
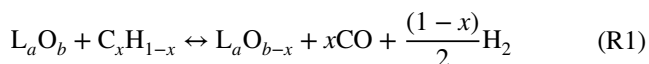
Table 6 Parameter estimates for Eq. (7) for the product selectivity ratio variation with respect to R_{CO_2} during oxidative dry reforming

Product ratio, $i{:}j$	PR_{ij}^{∞}	α_{ij}	β_{ij}	Correlation coefficient
$CH_4{:}CO$	0	0.90	1.50	0.99
$CH_4{:}H_2$	0	0.77	0.70	0.99
$H_2{:}CO$	0.36	0.89	0.64	0.99

$i,j = CH_4$, H_2 and CO

of lanthanide (L) promoters in redox reactions, L^{4+}/L^{3+}, for C_xH_{1-x} consumption during dry reforming has been proposed by [8], namely

Reducing step:

$$L_aO_b + C_xH_{1-x} \leftrightarrow L_aO_{b-x} + xCO + \frac{(1-x)}{2}H_2 \qquad (R1)$$

Re-oxidizing step:

$$L_aO_{b-x} + xCO_2 \leftrightarrow L_aO_b + xCO \qquad (R2a)$$
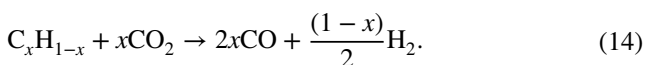
or

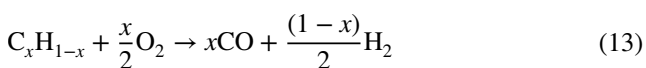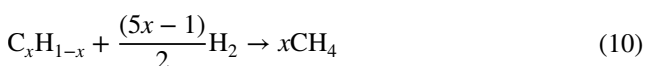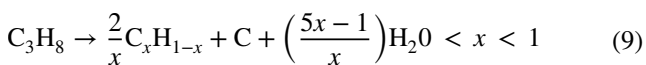$$L_aO_{b-x} + \frac{x}{2}O_2 \leftrightarrow L_aO_b \qquad (R2b)$$

where $a = 1$ or 2 and $b = 2$ or 3.

In view of these observations, the key steps during oxygen-assisted dry reforming may be proposed as the initial dehydrogenation of propane to H_2, atomic surface carbon, C, surface carbonaceous deposit, C_xH_{1-x} which undergoes hydrogenation to CH_4 followed by simultaneous oxidation of H_2, CH_4 and the residual surface C_xH_{1-x} species to water, CO and H_2. However, as the CO_2 partial pressure increased, reaction between deposited carbon and CO_2 would yield improved CO production. The additional oxidation of CO to CO_2 by oxygen is possible but has not been explicitly listed in view of the high partial pressure of CO_2 as R_{CO_2} increased. Consequently, the following reactions may be posited:

$$C_3H_8 \rightarrow \frac{2}{x}C_xH_{1-x} + C + \left(\frac{5x-1}{x}\right)H_20 \ <x<1 \qquad (9)$$

$$C_xH_{1-x} + \frac{(5x-1)}{2}H_2 \rightarrow xCH_4 \qquad (10)$$

$$C + \frac{1}{2}O_2 \rightarrow CO \qquad (11)$$

$$C + CO_2 \rightarrow 2CO \qquad (12)$$

$$C_xH_{1-x} + \frac{x}{2}O_2 \rightarrow xCO + \frac{(1-x)}{2}H_2 \qquad (13)$$

$$C_xH_{1-x} + xCO_2 \rightarrow 2xCO + \frac{(1-x)}{2}H_2. \qquad (14)$$

$$H_2 + \frac{1}{2}O_2 \rightarrow H_2O \qquad (15)$$

$$H_2 + CO_2 \rightarrow CO + H_2O. \qquad (16)$$

It has been assumed that CH_4 also goes through successive dehydrogenation similar to steps (9) to (14) and may be summarized as:

$$CH_4 + CO_2 \rightarrow 2CO + 2H_2 \qquad (17)$$

Dry partial oxidation runs: effect of oxygen co-feeding (R_{O_2})

The influence of O_2 addition during dry reforming was studied using a feed containing $CO_2{:}C_3H_8$ ratio, $R_{CO_2} = 1.5$. The experimental range for the $O_2{:}C_3H_8$ ratio, R_{O_2}, was 0–1.5 to avoid conditions for total hydrocarbon oxidation [cf. Eqn (8)]. Figure 5a shows the reaction rate envelopes for CO_2 and CO while the profiles for H_2, CH_4 and C_3H_8 are displayed in Fig. 5b. As may be seen in Fig. 5a, CO production rate peaked at R_{O_2} of about 0.75 while CO_2 consumption rate was initially flat but dropped at $R_{O_2} > 0.75$. However, in Fig. 5b, all three products appear to crest around the same feed O_2 partial pressure, $R_{O_2} = 0.75$ implicating similar rate-controlling steps. It would, therefore, seem that O_2 and C_3H_8 most likely chemisorb on similar sites, the electron-deficient metal–support interface centers. Indeed, the left skew of the rate-composition profiles indicates that O_2 was more strongly adsorbed than the hydrocarbon. The experimental heat of desorption for C_3H_8 was 74 kJ mol^{-1} in this study compared with 200 kJ mol^{-1} on Ni for O_2 [22].

The intercept on the rate-axis corresponding to the reaction rate value for pure dry reforming using $R_{CO_2} = 1.5$ suggests that the introduction of O_2 initially enhanced product formation rate as well as C_3H_8 consumption (with concurrent dry reforming) most likely through additional oxygen gasification of the surface carbon moieties [cf. Eqn (13)]. Alenazey et al. (2011) have demonstrated that O_2 is a more aggressive carbon gasifier than CO_2 and, hence, the steady rise in H_2, CH_4, C_3H_8 and CO rate as carbon-ladden metal sites was re-oxidized to the metal atoms, thereby improving catalyst activity in the region, $0 \leq R_{O_2} \leq 0.75$. Nevertheless, at $R_{O_2} > 0.75$, continuing oxidation probably caused metal site oxide formation resulting in a loss of catalyst activity which combined with a concomitant lowering of C_3H_8 partial pressure to reduce surface concentration of C_xH_{1-x} and the associated decline in species formation rate in this region, $0.75 \leq R_{O_2} \leq 1.5$. The earlier plateau in the CO_2 consumption rate curve indicates that carbon gasification via Eq. (14) was taking place at the constant R_{CO_2} value employed albeit the increased O_2 partial pressure was becoming a more significant contributor to species formation until at $R_{O_2} > 0.75$; CO_2 became rather uncompetitive with O_2 as the
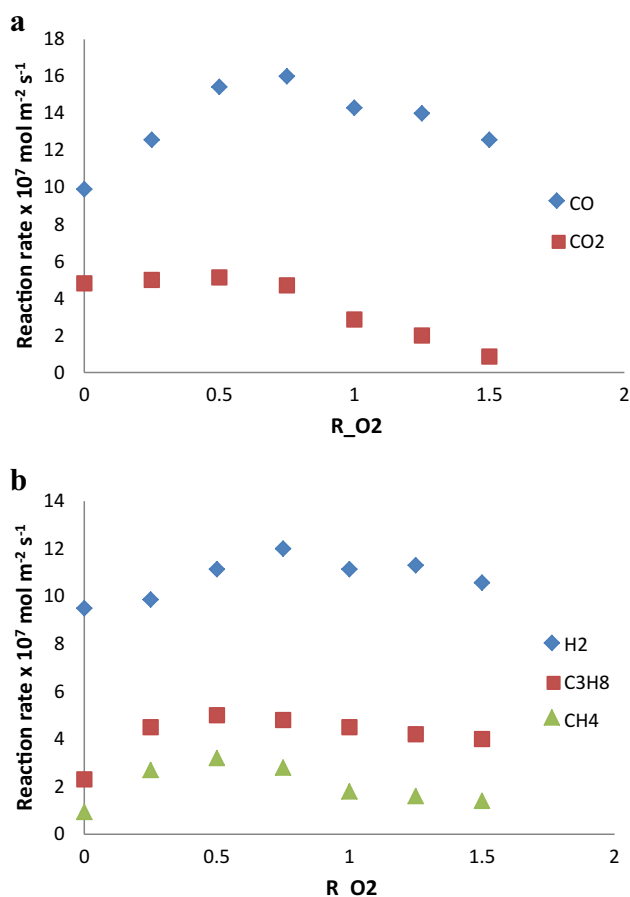
Fig. 5 **a** Reaction rate profiles for CO and CO_2 under dry partial oxidation using R_{CO_2} of 1.5 at 873 K. **b** Reaction rate profiles for H_2, C_3H_8 and CH_4 under dry partial oxidation using R_{CO_2} of 1.5 at 873 K

key oxidant for surface carbonaceous species. Hence, the drop in CO_2 consumption rate in the upper range was $0.75 \leq R_{O_2} \leq 1.5$.

As previously alluded to, the appearance of a maximum in the rate envelopes for H_2, CH_4, C_3H_8 and CO suggests the applicability of an empirical kinetic model similar to Eq. (5), namely

$$r_j\left[\text{or}\left(-r_j\right)\right] = \frac{\left[r_j^0 + k_3 R_{O_2}\right]}{\left[1 + k_4 R_{O_2}\right]^2} \quad j = H_2, \ CH_4, \ C_3H_8 \text{ and CO}$$

(18)

where, as before, k_3 is a pseudo-kinetic constant and k_4 is a combination of adsorption equilibrium constants in the steps for each of H_2, CH_4, C_3H_8 and CO production, while $R_{CO_2} = 1.5$. Table 7 contains the associated parameter estimates from the nonlinear regression fit of the data. The relatively low correlation coefficient values for H_2 and CH_4 (0.87 and 0.92, respectively) may be due to the inability of the model to comprehensively capture the secondary interaction between these two species, especially at near zero R_{O_2} values where secondary H_2 production from further CH_4 dehydrogenation was probably somewhat more dominant than reaction of either with O_2. Even so, this is not a significant impairment to the model fidelity.

The CO_2 rate profile with an initial plateau followed by a decline, however, is a characteristic inverted logistic behavior (the S-curve occurs frequently in natural processes where performance seemed stalled or latent at the beginning before an exponential acceleration/deceleration until maturity or termination eventuates (such as in complex learning/adaptation systems). These features capture the catalyst performance progression from a substantially dry reforming condition to the predominantly oxidation stage. Thus, the CO_2 rate data were fitted to the 3-parameter logistic model given by

$$\left(-R_{CO_2}\right) = \frac{r^{\max}}{\left[1 + \eta(R_{O_2})^v\right]}$$

(19)

where $r^{\max}$ is the maximum value for CO_2 consumption rate (during pure dry reforming, i.e., $R_{O_2} = 0$ and $R_{CO_2} = 1.5$) while η and v are model constants. Nonlinear regression of the rate data provides $r^{\max} = 5.05 \times 10^{-7}$ mol m^{-2} s^{-1}, $\eta = 0.58$ and $v = 5.14$ with a correlation coefficient of 0.991 implicating a good fit of the rate model.

Figure 6 illustrates the plots for product ratio trend with respect to the feed oxygen variable, R_{O_2}. Unlike the data in Fig. 4, where the H_2:CO ratio decreased almost exponentially with CO_2 partial pressure, Fig. 6 shows that this reaction index experienced an initial decrease going through a minimum at $R_{O_2} = 0.5$ before an upturn. Although both H_2 and CO rates exhibited an upward trend in the region, $0 \leq R_{O_2} \leq 0.5$, it would seem that CO production contributed via Eqs. (11) & (12) which were unaccompanied by stoichiometric H_2 production steps such as Eqs. (13) & (14) played a significant role leading to a declining trend in the H_2:CO ratio. However, a change in

Table 7 Parameter estimates for Eq. (18) for species reaction rate profiles during dry partial oxidation

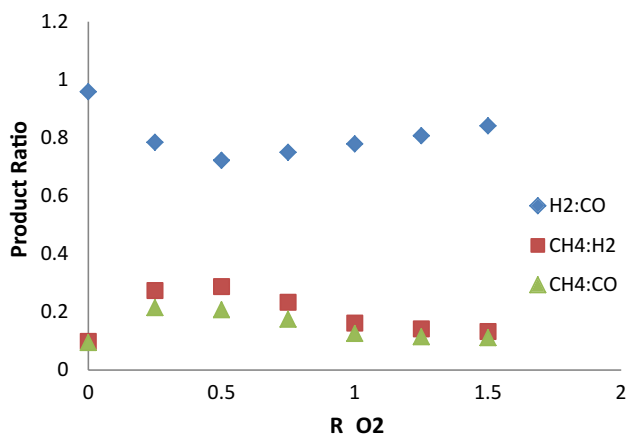| Species, j	$r_j^0 \times 10^7$ (mol m^{-2}s^{-1})	$k_3 \times 10^7$ (mol m^{-2} s^{-1})	k_4	Correlation coefficient
H_2	9.24	16.58	0.51	0.87
C_3H_8	2.30	23.99	1.47	0.99
CH_4	0.92	34.70	3.15	0.92
CO	9.61	45.74	0.95	0.97

Fig. 6 Product ratio profiles for dry partial oxidation using R_{CO_2} of 1.5 at 873 K

the rate-controlling step(s) for CO production is signaled at the minimum point where the reduction in coverage or absence of surface carbon atom, C, probably shut down CO contribution from Eqs. (11) & (12). Even so, H_2 and CO formation still continued via other steps such that the H_2:CO ratio now increased almost linearly over the range, $0.5 \leq R_{O_2} \leq 1.5$. Clearly, within the window, $0 \leq R_{O_2} \leq 0.5$, C_3H_8 partial pressure would be higher than in the upper O_2 range, $0.5 \leq R_{O_2} \leq 1.5$, making it more realistic that propane decomposition via Eq. (9) which produces atomic C as accompaniment to C_xH_{1-x} and H_2 would be more likely than the alternative decomposition step operative in the region, $0.5 \leq R_{O_2} \leq 1.5$, namely

$$C_3H_8 \rightarrow \frac{2}{x}C_xH_{1-x} + CH_4 + (1+x)H_2. \quad (20)$$
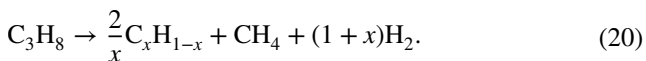
where C is not formed. Equations (9) and (20) also suggest that the empirical composition of the C_xH_{1-x} adspecies depends, in part, on the hydrocarbon feed composition. This has also been experimentally corroborated by Hardiman et al. [14]. Thus, the H_2:CO product ratio over the entire R_{O_2} range may be captured by the linear combination of the two regimes as:

$$PR_{i:j} = \frac{\alpha_{ij}}{(1 + \beta_{ij}R_{O_2})} + \lambda_{ij}R_{O_2} \quad (21)$$

where $i:j = H_2$:CO, α_{ij}, β_{ij} and λ_{ij} are non-negative model parameters. We note that α_{ij} is the H_2:CO ratio for pure (O_2-free feed) dry reforming using $R_{CO_2} = 1.5$. Estimates of these model constants based on data regression to Eq. (21) are provided in Table 8.

The curves for CH_4:CO ratio and CH_4:H_2 ratio shown in Fig. 6 are nearly parallel to peaks co-located at $R_{O_2} = 0.5$. Although differing in magnitude, the observed trends for the

Table 8 Parameter estimates for Eq. (22) for the product selectivity ratio variation with respect to R_{O_2} during dry partial oxidation

Product ratio, $i{:}j$	PR_{ij}^0 or λ_{ij}	α_{ij}	β_{ij}	Correlation coefficient
CH_4:CO	0.094	2.73	3.48	0.98
CH_4:H_2	0.098	3.95	3.71	0.96
H_2:CO**	0.37	0.95	1.45	0.98

**The expression for H_2:CO product ratio is given by Eq. (21)

two profiles invite the application of a common nonlinear model:

$$PR_{i:j} = \frac{[PR_{ij}^0 + \alpha_{ij}R_{O_2}]}{[1 + \beta_{ij}R_{O_2}]^2} \quad i, j = H_2, CH_4 \text{ and CO} \quad (22)$$

with PR_{ij}^0 as the product ratio of i to j at $R_{O_2} = 0$ (i.e., pure dry reforming using $R_{CO_2} = 1.5$), while α_{ij} and β_{ij} are empirical constants associated with the formation rate of species i and j. Regression analysis of the product selectivity ratio data yielded the parameter estimates in Table 8.

Figure 7 illustrates the Arrhenius plots for the reaction specs. Activation energy values for H_2, CO, CO_2 and CH_4 were obtained as 30.2, 30.5, 45.3 and -127 kJ mol^{-1}, respectively. The similarities in magnitude of the activation energy estimates for H_2, CO and CO_2 suggest that their production may not be the rate-determining step in the complex reaction network. However, the negative activation energy for CH_4 confirms its linkage with the carbon deposition step [cf. Eqn (9)]. Bartholomew [4] found that carbon deposition rate (from alkanes) decreased with increasing temperature in the range 773–873 K. As a result, CH_4 formation from Eqs. (9) to (10) would be characterized by negative activation energy as obtained in this case. Indeed, Hardiman et al. [14, 15] have reported a similar observation in their steam reforming investigation
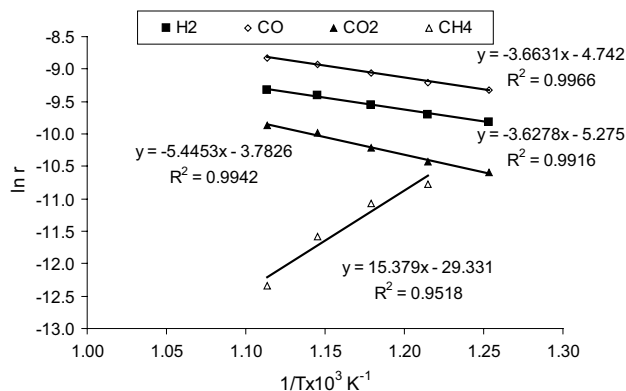

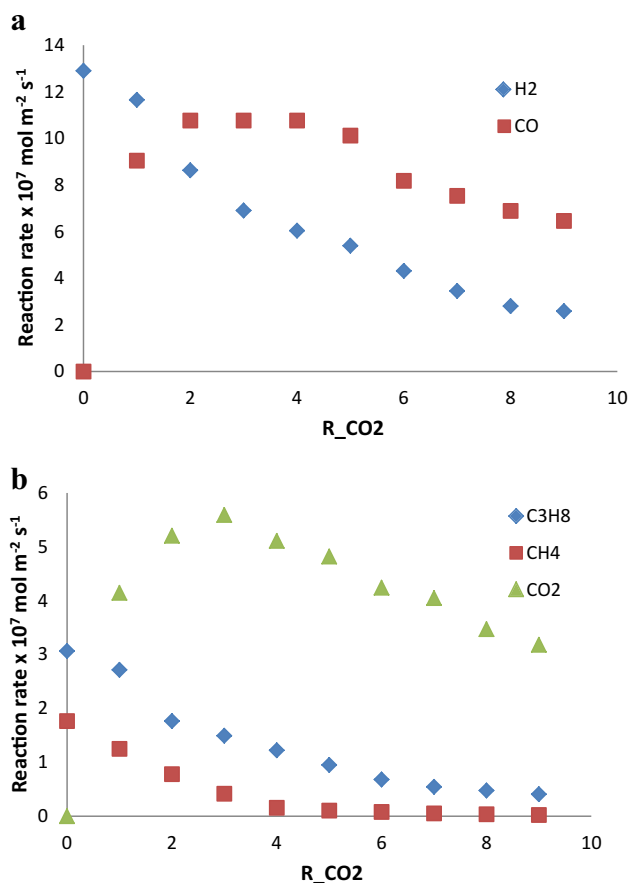**Fig. 7** Arrhenius plots for the reaction species using R_{CO_2} of 4.0 and R_{O_2} of 1.5

a

b

Fig. 8 **a** Reaction rate profiles during pure dry reforming at 873 K. **b** Reaction rate profiles during pure dry reforming at 873 K

Table 9 Estimates of parameters for Eq. (4) based on the rate profiles for H_2, CH_4 and C_3H_8 during pure dry reforming

Species, i	$r_i^0 \times 10^7$ (mol m^{-2} s^{-1})	K_{DR}	Correlation coefficient
H_2	13.77	0.34	0.98
CH_4	1.84	1.05	0.95
C_3H_8	3.28	0.46	0.97

$i = H_2$, CH_4 and C_3H_8

Table 10 Estimates of parameters for Eq. (5) using the CO and CO_2 rate data for pure dry reforming

Species	$r_j^0 \times 10^7$ (mol m^{-2} s^{-1})	$k_1 \times 10^7$ (mol m^{-2} s^{-1})	k_2	Correlation coefficient
CO	0.02	19.65	0.45	99
CO_2	0	8.86	0.42	0.99

$j = CO$ and CO_2
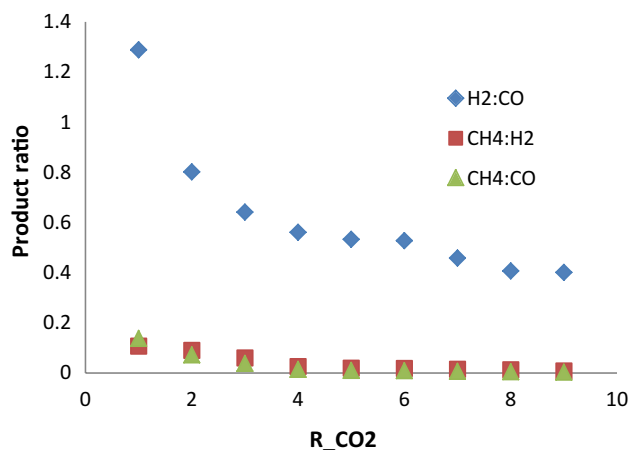
Fig. 9 Product ratio profiles during pure dry reforming at 873 K

at low feed steam:propane ratio. Eqn (9) would, therefore, appear to be one of the kinetically dominant reaction steps in this study. Even so, it is instructive that all rate data used have been checked for the absence of negligible transport resistances [7].

Comparison between the oxygen-containing runs with pure dry reforming

Figure 8a, b shows the reaction rate profiles under conventional dry reforming conditions. While H_2 and CH_4 production as well as C_3H_8 utilization rates decreased exponentially with increased CO_2 partial pressure, the rate profiles for CO, CO_2 are characterized by an optimum at $R_{CO_2} = 3$ suggesting conformity with stoichiometric requirements. However, the rate values at $R_{CO_2} = 0$ suggest that the direct decomposition of C_3H_8 produced only H_2 and CH_4 with practically no CO formation. This indicates that ceria participation as an oxygen source was not significant suggesting that the redox reaction involving the promoter is triggered only in the presence of a gas phase

oxygen carrier (such as CO_2 or O_2) as described by redox equations (R1) to (R2). Furthermore, a CH_4:C_3H_8 ratio of 0.58 during decomposition implicates substantial carbon deposit on the catalyst surface. As may be expected, this ratio decreased with increased CO_2 partial pressure as later substantiated by carbon content analysis of the used catalyst. Not surprisingly, the C_3H_8, H_2 and CH_4 rate dependency on R_{CO_2} was captured by Eq. (4) where K_{oxi} has been substituted for K_{DR} in the denominator. However, the unimodal behavior describing the CO and CO_2 rate was adequately depicted by Eq. (5). The relevant parameter estimates from regression analysis are provided in Tables 9 and 10. Figure 9 also displays the product selectivity ratio under pure dry reforming conditions. The hyperbolic decay pattern is similar to what was observed

Table 11 Parameter estimates for Eq. (22) for the product selectivity ratio variation with respect to R_{CO_2} during pure dry reforming

Product ratio, i:j	PR_{ij}^{∞}	α_{ij}	β_{ij}	Correlation coefficient
CH_4:CO	0	1.07	5.67	0.99
CH_4:H_2	0	0.22	0.44	0.97
H_2:CO	0.31	15.72	15.06	0.99

$i,j = CH_4$, H_2 and CO

during oxidative dry reforming in Fig. 4. As a result, the 3-parameter hyperbolic decay model given by Eq. (7) was also used to fit the data. The resulting parameter estimates are listed in Table 11.

Based on the foregoing discussion, the introduction of a specified O_2 dosage into the C_3H_8/CO_2 feed mixture enhanced catalyst performance through increased carbon gasification (with O_2), presumably via the same rate-controlling step(s) applicable during pure dry reforming. However, the reaction behavior during dry partial oxidation was influenced by the stronger O_2 chemisorption and, hence, the reduced surface coverage of C_xH_{1-x} species needed for product formation resulted in unimodal rate profiles for all reaction products.

Although the three sets of experiments reported in this study have employed different feed conditions (O_2-dosed dry reforming, CO_2-dosed partial oxidation and pure dry reforming), the participation of common reacting species, namely CO_2, C_3H_8, O_2, H_2 and CH_4 over the same catalyst allows some important comparisons to be made with respect to role of feed CO_2:O_2 ratio in determining the relative significance of steps involved in oxygen-assisted hydrocarbon reforming, trend and magnitude of product selectivity ratio as well as possible switching of rate-controlling steps. It is apparent from Figs. 10a, b which pool together the rate data for oxidative dry reforming and dry partial oxidation that the individual species rate has a discernible dependency on the CO_2:O_2 feed ratio implying that the reaction pathway illustrated by Eqs. (9)–(17) provides a plausible account of product formation even if different rate-limiting steps may be necessary for individual components.

The rapid decay of the H_2 formation rate with increasing CO_2:O_2 feed ratio is consistent with the consumption of initial H_2 production (via C_3H_8 decomposition on the reduced metal sites) with both CO_2 and O_2 as required by Eqs. (15)–(16). On the other hand, the profiles for both C_3H_8 and CH_4 in Fig. 10a exhibit peaks at about CO_2:O_2 feed ratio of about three implicating similarity in rate-controlling steps for these two species. In particular, the existence of a peak in the rate profile means that two surface entities were involved in rate-determining step. In the case of C_3H_8, this may be conjectured as the two vacant metal sites required
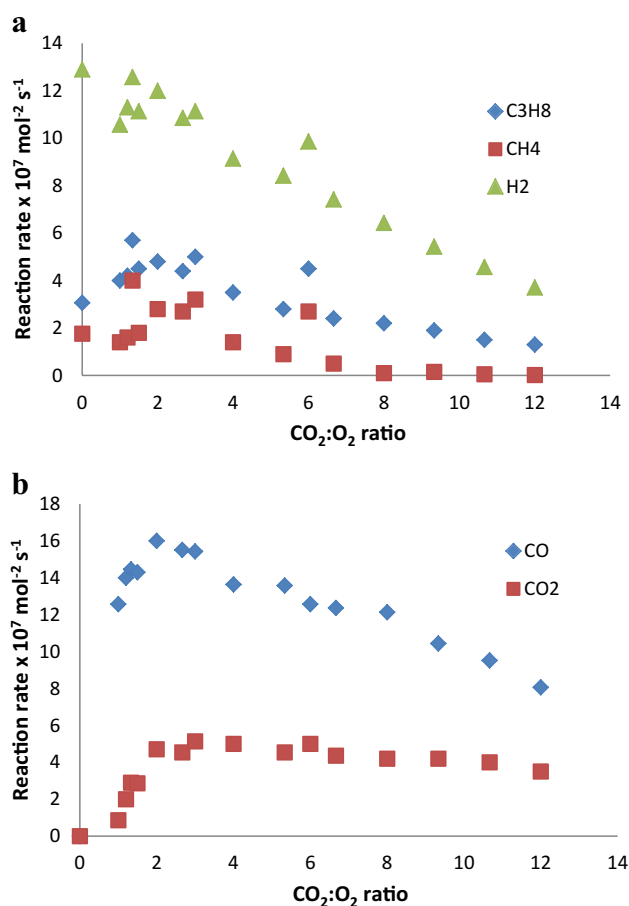
Fig. 10 a Reaction rate envelope as a function of the feed CO_2:O_2 ratio across the oxidative dry reforming and dry partial oxidation conditions at 873 K. **b** Reaction rate envelope as a function of the feed CO_2:O_2 ratio across the oxidative dry reforming and dry partial oxidation conditions at 873 K

for dissociative chemisorption. For CH_4 formation, the rate-limiting step would be the surface hydrogenation of C_xH_{1-x} species. By same token, the CO and CO_2 rate envelopes in Fig. 10b suggest a commonality between the controlling steps for CO production and CO_2 utilization with both curves having their individual maximum at CO_2:O_2 feed ratio = 3.

Product selectivity ratio considerations also reveal that the H_2:CO ratio has a relatively small variability (0.72–0.96 with an average value of 0.81) for the dry partial oxidation runs than the wide variation observed (0.48–1.25 with an average of 0.68) for the oxidative dry reforming. This would suggest that the dry partial oxidation mode of operation should be more suited for syngas produced as feed to olefin manufacturing Fischer–Tropsch plants. In general, however, H_2 and CO production rates were about the same magnitude for both types of operation with the dry partial oxidation exhibiting milder
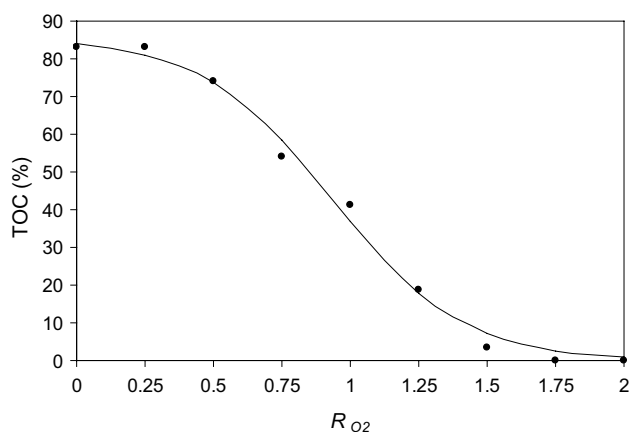
variation than the oxidative dry reforming. Interestingly, the pure dry reforming H_2 and CO production rates too are in the same size range as the two forms of O_2-assisted dry reforming modes. Nonetheless, the DPOX runs have superior heat utilization as thermodynamics calculations indicate.

Post-reaction carbon analysis

The residual carbon content on the used catalysts from the DPOX runs is plotted in Fig. 11. The high total organic carbon (TOC) content registered in the low R_{O_2} region is consistent with the previous discussion regarding high propane dehydrogenation to surface C_xH_{1-x} at low R_{O_2}. The sigmoid exhibited a rapid drop in region $0.5 \leq R_{O_2} \leq 1.25$ which incidentally corresponds to the zone where maximum reaction rate occurred. It would seem that a more resistant carbonaceous deposit was formed at low R_{O_2} while under O_2-rich conditions a more reactive carbon was present. Hardiman et al. [15] conducted temperature-programmed oxidation–reduction experiments to characterize coke on used catalysts from propane steam reforming and confirmed the existence of both naphthalenic and aliphatic C_xH_{1-x} species on the used samples. A similar observation was also reported during propane dry reforming over unpromoted Co–Ni catalyst [3]. The left-sided S-curve seen in Fig. 11 is a reflection of the different reactivities with oxygen for these two forms of carbonaceous pool. Even so, the S-shaped TOC(%) profile across the range of R_{O_2} values used in this study may be captured by the 3-parameter sigmoid expression:

$$\text{TOC} = \frac{A_{\text{TOC}}}{\left\{1 + e^{\rho\left(R_{O_2} - R_{O_2}^{\text{crit}}\right)}\right\}}. \tag{23}$$

where A_{TOC} is the catalyst capacitance for carbon deposition, while ρ is the oxygen-induced anti-coking factor for the catalyst and $R_{O_2}^{\text{crit}}$ is the critical O_2:C_3H_8 ratio when TOC is at 50% of A_{TOC} (and it is the point at which the transition occurs from one type of coke to another in this case). Nonlinear regression of the data gave parameter estimates for A_{TOC}, ρ and $R_{O_2}^{\text{crit}}$ as: 85.61%, 4.17, and 0.93, respectively. Alenazey et al. [2] have shown that the value of $R_{O_2}^{\text{crit}}$. depends on the type of carbon gasification agent (where O_2 may be replaced by the required gasifying agent) used for the coke removal.

Conclusions

For the first time, a study of the oxygen-assisted dry reforming of propane has been carried out using Ce-promoted Co–Ni/Al_2O_3. Catalyst characterization revealed that the common physicochemical properties (BET area, pore volume, H_2 chemisorption) of the Ce-promoted and undoped catalysts were essentially the same with the exception of the increase in surface basicity (as measured by NH_3 and CO_2 temperature-programmed desorption) of the ceria-containing sample. XRD pattern confirmed the presence of a CeO_2 phase in the latter catalyst. Dry partial oxidation (CO2-dosed partial oxidation) appeared to be superior to both oxidative dry reforming and pure dry reforming in terms of the value and uniformity in H_2:CO product ratio if the syngas is to be employed for olefin or GTL manufacture. Reaction runs with varying oxygen partial pressure showed that even with a low CO_2:C_3H_8 ratio ($R_{CO_2} = 1.5$) where carbon deposition was significant, the addition of O_2 improved the H_2:CO ratio in the product stream above that obtained for pure dry reforming. Furthermore, analysis of the TOC content in the used catalysts points to the beneficial effects of autodry reforming operation in terms of significant reduction in carbon residue and, thus, the increased longevity of the catalyst. Kinetics of the product formation may be classified into two generic types, namely a hyperbolic decay dependency on R_{CO_2} (for H_2, CH_4 and C_3H_8) and a Langmuir–Hinshelwood type relation (for CO and CO_2) during oxidative and pure dry reforming reactions. The rate behavior of participating species during dry partial oxidation was determined by different rate-limiting steps since the form of the Langmuir–Hinshelwood rate model involves the interaction of two surface entities in the rate-controlling step (an exponent of two for the denominator).

References

1. Adesina AA (2012) The role of CO_2 in hydrocarbon reforming catalysis: friend or foe? Curr Opin Chem Eng 1:272–280
2. Alenazey F, Cooper CG, Dave CB, Elnashaie SSEH, Susu AA, Adesina AA (2009) Coke removal from deactivated Co–Ni catalyst using different gasifying agents: an analysis of the gas–solid reaction kinetics. Catal Commun 10:406–411
3. Althenayan FM, Foo SY, Kennedy EM, Dlugogorski BZ, Adesina AA (2010) Bimetallic Co–Ni/Al_2O_3 catalyst for propane dry reforming: estimation of reaction metrics from longevity runs. Chem Eng Sci 65:66–73
4. Bartholomew CH (2001) Mechansims of catalyst deactivation. Appl Catal A 212:17–60
5. Buyeskaya OV, Wolf D, Baerns M (2000) Ethylene and propene by oxidative dehydrogenation of ethane and propane: `performance of rare-earth oxide-based catalysts and development of redox-type catalytic materials by combinatorial methods'. Catal Today 62:91–99
6. Emeis CA (1993) Determination of integrated molar extinction coefficients for infra red absorption bands of pyridine adsorbed on solid acid catalysts. J Catal 141:347–354
7. Fogler HS (1999) Elements of chemical reaction engineering. Prentice-Hall, Englewood
8. Foo SY, Cheng CK, Nguyen TH, Adesina AA (2011) Evaluation of lanthanide-group promoters on Co–Ni/Al_2O_3 catalysts for CH_4 dry reforming. J Mol Catal A 344:28–36
9. Foo SY, Chen CK, Nguyen TH, Kennedy EM, Dlugogorski BZ, Adesina AA (2012) Carbon deposition and gasification kinetics of used lanthanide-promoted Co–Ni/Al_2O_3 catalysts from CH_4 dry reforming. Catal Commun 26:183–188
10. Gao J, Guo J, Liang D, Hou Z, Fei J, Zheng X (2008) Production of syngas via autothermal reforming of methane in a fluidized bed reactor over CeO_2–ZrO_2/SiO_2 supported Ni catalysts. Int J Hydrogen E 33:5493–5500
11. Glockler B, Gritsch A, Morillo A, Kolios G, Eigenberger G (2004) Autothermal reactor concepts for endothermic fixed-bed reactions. Chem Eng Res Des 82:148–159
12. Guo J, Hou Z, Gao J, Zheng X (2008) Syngas production via combined oxy-CO_2 reforming of methane over Gd_2O_3-modified Ni/SiO2 catalysts in a fluidized bed reactor. Fuel 87:1348–1354
13. Guo J, Hou Z, Gao J, Zheng X (2008) Production of syngas via partial oxidation and CO_2 reforming of coke oven gas over a Ni catalyst. Energy Fuels 22:1444–14448
14. Hardiman K, Ying T, Adesina AA, Kennedy EM, Dlugogorski BZ (2004) Performance of a Co–Ni catalyst for propane reforming under low steam-to-carbon ratios. Chem Eng J 102:119–130
15. Hardiman K, Cooper CG, Adesina AA, Lange R (2006) Post-mortem characterization of coke-induced deactivated alumina-supported Co–Ni catalysts. Chem Eng Sci 61:2565–2573
16. Holladay JD, Hu J, King DL, Wang Y (2009) An overview of hydrogen production technologies. Catal Today 139:244–260
17. Kolios G, Frauhammer J, Eigenberger G (2000) Autothermal fixed-bed reactor concepts. Chem Eng Sci 55:5945–5967
18. Ma L, Jiang C, Adesina AA, Wainwright MS, Trimm DL (1996) Simulation studies of autothermal reactor system for H_2 production from methanol steam reforming. Chem Eng J 62:103–111
19. Mohamedali M, Henni A, Ibrahim H (2018) Recent advances in supported metal catalysts for syngas production from methane. Chem Eng 2:9–32
20. Natesakhawat S, Oktar O, Ozkan US (2005) Effect of lanthanide promotion on catalytic performance of sol–gel Ni/Al_2O_3 catalysts in steam reforming of propane. J Mol Catal A 241:133–146
21. Pena MA, Gomez JP, Fierro JLG (1996) New catalytic routes for syngas and hydrogen production. Appl Catal A 144:7–57
22. Sachtler WMH, Reijen L (1962) Chemisorption bonds on metals. J Res Inst Catalysis Hokkaido Univ 10:87–104
23. Sengodan S, Lan R, Humphreys J, Du D, Xu W, Wang H, Tao S (2018) Advances in reforming and partial oxidation of hydrocarbons for hydrogen production and fuel cell applications. Renew Sustain Energy Rev 82:761–780
24. Shahid G, Sheppard N (1990) Infrared spectra and the structures of the chemisorbed species resulting from the adsorption of propene and propane on a Pt/SiO2 catalyst. Spectrochim Acta A 46:999–1010
25. Sheppard N (1988) Vibrational spectroscopic studies of the structure of species derived from chemisorption of hydrocarbons on metal single-crystal surfaces. Ann Rev Phys Chem 39:589–644
26. Suthinmporn K, Kawi S (2011) Promotional effect of alkaline earth over Ni–La_2O_3 catalyst for CO_2 reforming of CH_4: role of surface oxygen species on H_2 production and carbon suppression. Int J Hydrogen Energy 36:14435–14446
27. Wang Y, Yao L, Wang S, Mao D, Hu C (2018) Low-temperature catalytic CO_2 dry reforming of methane on Ni-based catalysts: a review. Fuel Proc Tech 169:199–206
28. Wilhelm DJ, Simbeck DR, Karp AD, Dickenson RL (2001) Syngas production for gas-to-liquids applications: technologies, issues and outlook. Fuel Proc Tech 71:139–148
29. Zhang J, Wang H, Dalai AK (2007) Development of stable bimetallic catalysts for carbon dioxide reforming of methane. J Catal 249:300–310